Combining experiments and simulations to study the impact of multiple phosphorylations at the AT8 epitope of the Tau protein

Cynthia Lohberger[1¶], Jules Marien[2¶], Clarisse Bridot[3], Chantal Prévost[2], Diane Allegro[1], Mario Tatoni[4], Emmanuelle Boll[3], François-Xavier Cantrelle[3], Marlène Martinho[4], Valérie Belle[4], Caroline Smet-Nocca[3], Sophie Sacquin-Mora[2*] and Pascale Barbier[1*]

Affiliations :

1. Aix Marseille Univ, CNRS, Institut de Neurophysiopathologie, INP, UMR7051, Marseille, 13005, France.

2. IBPC, Laboratoire de Biochimie Théorique, Université Paris Cité, CNRS, 75005, Paris, France.

3. INSERM U1167, Université de Lille, Lille, 59000, France.

4. Aix Marseille Univ, CNRS, Bioénergétique et Ingénierie des Protéines, BIP UMR 7281, IMM, IM2B, Marseille, 13009, France.

* Correspondence: pascale.barbier@univ-amu.fr, sacquin@ibpc.fr.

These authors contributed equally to this work.

Running title : Conformation of phosphorylated AT8-Tau

A preliminary version of this work was deposited in BioRxiv, doi:

https://doi.org/10.1101/2025.02.22.639620

Abstract

The Intrinsically Disordered Protein (IDP) Tau is, under a hyperphosphorylated form, one of the molecular hallmarks of Alzheimer's disease. This abnormal phosphorylation induces both a functional loss to regulate microtubule assembly and the formation of intraneuronal fibrillar inclusions. Notably, phosphorylation sites recognized by the AT8 antibody are particularly relevant in the development of Alzheimer's disease. The main objective of this work is to understand how AT8 phosphorylation site affects the conformation and dynamics of Tau protein as early steps in Tau pathological transformation. We engineered an alanine Tau mutant to target specific phosphorylation sites restricted to the AT8 epitope, for which we generated two distinct phosphorylation states differing by the number of phosphosites. The combination of Dynamic Light Scattering (DLS), Analytical UltraCentrifugation (AUC) and pCALVADOS (a forcefield based on CALVADOS 2 with phosphorylation-specific parameters) allowed us to determine that both alanine mutation and phosphorylation on the AT8 epitope do not significantly change the hydrodynamic radius of the conformational ensemble. Our calculations of Local Curvatures and Local Flexibilities corroborated by cw EPR experimental data indicated that the mutations for selective phosphorylation did not modify Tau's global dynamics. Nevertheless, simulations revealed that local stiffening and extension at the AT8 epitope scale with the extent of phosphorylation. Interestingly, phosphorylation does not just affect the immediate AT8 area but leads to distant contact losses, directed towards the N-terminus, potentially influencing Tau's function. The study paves the way for future research on Tau's

structure-function-dynamics relationship and the role of phosphorylation in neurodegenerative diseases.

Keywords: Molecular dynamics, Tau protein, phosphorylation, IDP, Alzheimer disease, hydrodynamic radius, AT8 epitope, coarse-grained force field.

Statement of significance

We combined experimental and simulation approaches to investigate the role of Tau site-specific protein phosphorylation at the AT8 epitope, which is implicated in Tau transformation associated with Alzheimer's disease. We demonstrated that while phosphorylation does not significantly alter the overall size of Tau, it induces local structural changes at the AT8 epitope and long-range contact losses. These findings suggest a potential mechanism in which specific phosphorylation could modulate Tau's interactions and function, contributing to neurodegeneration. Combining experimental studies with the pCALVADOS model, we provided a robust approach for future studies on Tau's structure-function-dynamics and more generally for studying intrinsically disordered proteins and the impact of post-translational modifications on their conformational ensembles.

Introduction

Alzheimer's disease (AD) is characterized by the presence of two key biomarkers: extracellular amyloid plaques formed by the accumulation of β-amyloid fibrils, and intracellular neurofibrillary tangles composed of aggregated hyperphosphorylated Tau protein, along with neurodegeneration [1]. Tau is an intrinsically disordered protein belonging to the microtubule-associated protein family [2]. The physiological role of Tau in stabilizing axonal microtubules, thereby ensuring proper neuronal activity, is mediated by its interaction with tubulin via the C-terminal MicroTubule-Binding Domain (MTBD) and a region within the Proline Rich Domain (PRD) [3]. While phosphorylation regulates this physiological function, it is also a critical factor in the pathological aggregation of Tau into neurofibrillary tangles.

In the central nervous system, Tau exists as six isoforms ranging from 352 to 441 amino acids, generated by differential splicing resulting in variations in the N-terminal domain (0N, 1N, 2N) combined with different numbers of MTBD repeats that are composed of three or four imperfectly repeated sequences of 18 residues (3R, 4R) [4]. Phosphorylation within the PRD has been shown to be involved in Alzheimer's disease (AD) [5]. Building upon this clinical relevance, the present study focuses on pathological phosphorylations of Tau recognized by the AT8 antibody at Serine 202, Threonine 205, and Serine 208 [6]. We chose these specific phosphorylation sites as the AT8 antibody is commonly used in post- mortem diagnosis of Alzheimer's disease and its staining on patients' brains correlates with the different Braak stages defining the disease progression [7]. To isolate the effects of three and five specific phosphorylations including AT8 epitope, we used a Tau isoform in which 16

NMR-characterized phospho-sites were mutated to Alanine to abolish their phosphorylation by CDK2/cyclin A and GSK3β kinases. We define these phosphorylation states as p-state 1 (Serine 202, Threonine 205, and 212 are phosphorylated: pS202 + pT205 + pT212) and p-state 2 (p-state 1 with additional phosphorylation on Serine 198 and 208; pS198 + pS202 + pT205 + pS208 + pT212) (Fig 1 and S1) and compare them to the unphosphorylated AT8 mutant. Previous NMR structural studies have revealed that pS202/pT205/pT212 in p-state 1 induces a local conformational change characterized by a kink at residue G207. Interestingly, this kink is disrupted by the additional phosphorylation of Serine 208 [8,9]. Furthermore, while pS202/pT205 is unable to form oligomers, the triple phosphorylation pS202/pT205/pS208 exhibits a propensity to form pathological oligomers [8,9]. These findings suggest that the phosphorylation of Serine 208 plays a critical role in promoting detachment from microtubules and Tau aggregation, thereby contributing to the pathogenesis of neurodegenerative diseases by local conformational modification [10]. To assess the impact of this local conformational change on the overall conformation and dynamics of Tau, we combined experimental and simulation studies to determine the effect of multiple and specific phosphorylation on the local and global dynamics of Tau. After the control of the specific phosphorylation sites by NMR studies, hydrodynamic radii were measured by Dynamic Light Scattering (DLS) and Analytical UltraCentrifugation (AUC). Additionally, Site-Directed Spin Labeling combined with EPR spectroscopy was used to probe the local dynamics around the AT8 epitope comparing unphosphorylated AT8 mutant to p-state 1 and p-state 2. Furthermore, Molecular Dynamics (MD) simulations have been proved to be a method of choice to study the impact of mutations or post-translational modifications on the conformational dynamics of

proteins. However, simulating long IDPs via MD has proven to be a significant challenge due to their rugged conformational space and their large fluctuations in size. Coarse-grained models are promising attempts to generate Conformational Ensembles (CoE) at low computational cost compared to all-atom simulations. A popular type of force fields are ones based on the HydroPhobicity Scale (HPS) model by Kapcha and Rossky [11], among which the machine-learned CALVADOS FF is becoming a staple in the field [12]. However, the phosphoparameters by Rauh et al. [13] did not yet exist when performing the simulations of the present article, we thus assembled a new forcefield named pCALVADOS from Perdikari et al. phosphoparameters [14] and performed simulations matching the experimental sequences.

The computational assessment of the local dynamics of an IDP is a complex task as standard alignment-based methods such as RMSD and RMSF lose all meaning in disordered systems. We thus employed new metrics developed by Marien et al. [15] and specifically tailored for IDPs and IDRs (Proteic Menger Curvature, Local Curvature and Local Flexibility) [16].

Altogether, all data corroborated the absence of impact of the different phosphorylation states on the global shape and dynamics of Tau. Nevertheless, simulations allowed us to identify local stiffening and extension increasing with the phosphorylation states. Interestingly, phosphorylation goes beyond the immediate AT8 region, revealing distant contact losses, directed towards the N-terminus, potentially influencing Tau's function.

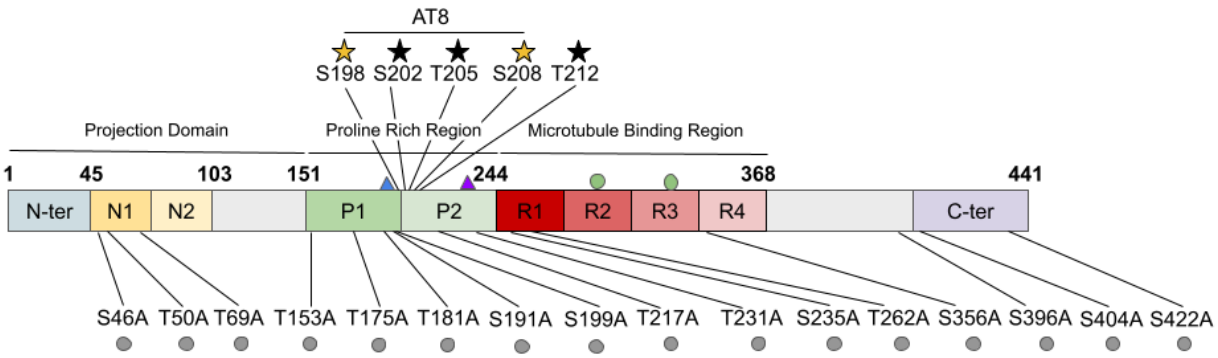

Fig 1: Domain organization and phosphorylation sites of wild-type longest human Tau isoform and its mutants designed to investigate the role of specific phosphorylation events in Alzheimer's disease. The gray circles represent the 16 Serines/Threonines mutated into Alanine. p-state 1: Serine 202 and Threonines 205 and 212 are phosphorylated indicated by black stars. p-state 2: Serines 198 and 208 are additionally phosphorylated compared to p-state 1 indicated by yellow stars. Additional mutations for Site-Directed Spin Labeling EPR Experiments are indicated: green dots for the two natural cysteines (C291 and C322) mutated in Alanine and triangles the introduced cysteines: (S185C, blue) and (A227C, purple).

Materials and methods

WT Tau purification

Tau purification has been already described [17,18] but we will summarize the main step here. The Tau-441 human (hTau40, 2N4R) gene was cloned into a pET-3d vector. This plasmid was transformed into *E. coli* BL21(DE3) cells. The bacteria were

grown overnight in a LB medium containing 100 µg/mL ampicillin for antibiotic selection. After dilution, the culture was supplemented with 20 mM glucose to promote growth. The Tau protein production was induced with 0.75 mM isopropyl 1-thio-β-D- galactopyranoside (IPTG) and cells were further incubated for 2 hours 30 min at 37 °C. The cells were harvested by centrifugation at 5000*x g* for 10 mins at 4 °C and then suspended in 2-(N-Morpholino)ethanesulfonic acid 45 mM, Triton X 100 8 mM, DTT 1mM, pH=3.8. The cell suspension was disrupted using a French press, releasing the cellular contents. The lysate was then heated to denature unwanted proteins and clarified by centrifugation at 30000*x g* during 30 min, separating soluble proteins from cell debris. The supernatant containing thermoresistant proteins and Tau was purified using a cation-exchange chromatography column HiTrap SP-HP 5 mL (Cytiva). The column was equilibrated with 45 mM MES, at pH 6.5, and loaded with the supernatant and then a salt gradient was applied. Tau protein bound to the column was eluted with 0.25 M of NaCl. The eluted fractions containing Tau were pooled together. To remove salt excess, the pooled fractions were dialyzed overnight against pure water. The purity of the proteins was verified by SDS-PAGE (Fig S1A). Finally, the Tau protein solution was lyophilized (freeze- dried) for storage.

Purification and characterization of phosphorylated and unphosphorylated AT8 mutants

The Tau AT8 mutant protein corresponds to a mutated form of Tau 2N4R isoform in which 16 Serine/Threonine were mutated into Alanine to prevent phosphorylation while keeping those of the AT8 phospho-epitope (S202, T205, S208), S198 and T212 [9] (Fig S2). The mutated serine/threonine sites are designed on the basis of the phosphorylation status determined by NMR experiments of hTau40 using

recombinant CDK2/cyclinA and GSK3β kinases in vitro [9,19]. The mutant was obtained by gene synthesis with optimization of codons for *E. coli* expression and cloned into the pET15b vector (Novagen) into NcoI/XhoI allowing removal of the sequence coding for the polyhistidine tag [19]. ^{15}N or $^{15}N,^{13}C$-labeled proteins were produced for functional assays and NMR analyses. Briefly, BL21(DE3) *E. coli* strains transformed with Tau mutants were grown in M9 minimal medium enriched with ^{15}N as nitrogen source for uniform isotopic ^{15}N-labelling (6g Na_2HPO_4, 3g KH_2PO_4, 0.5g NaCl, 4g glucose, 1g $^{15}NH_4Cl$, 0.5g ^{15}N-ISOGRO®, 1 mM $MgSO_4$, 100 µM $CaCl_2$, 100 mg ampicillin per liter) at 37°C. For $^{15}N,^{13}C$-labeling, the medium was prepared the same way with 2g $^{13}C_6$-glucose and 0.5g $^{15}N,^{13}C$-ISOGRO®. The protein expression was induced by addition of 0.5 mM IPTG for 3 hours. After harvesting the bacteria, the protein was purified by heating the soluble extract at 80°C for 15 minutes followed by cation exchange chromatography (CEx). Then, the CEx fractions were purified by reverse phase HPLC on a Zorbax C8-300SB column (Agilent) using a linear gradient of acetonitrile. The fractions containing the full-length TauAT8 protein were lyophilized, desalted into 20 mM NaPi buffer pH=6.5, dialyzed in water at 4°C overnight, and lyophilized again.

Phosphorylated forms of TauAT8 mutant were produced either by phosphorylation with recombinant CDK2/cyclinA (p-state 1, pS202 + pT205 + pT212) or by a sequential phosphorylation with CDK2/cyclinA and GSK3β kinases (p-state 2, pS198 + pS202 + pT205 + pS208 + pT212) as described in [19].

The Tau AT8 mutant and its two phosphorylated forms were analyzed by MALDI-TOF MS (Axima Assurance, Shimadzu) in a linear positive ion mode with sinapinic acid matrix after ZipTip®-C_4 desalting (Millipore). For the calculation of overall phosphorylation levels, a m/z increment of +80 Da per phosphate group was

measured and confirmed by SDS-Page (Figs S2). An NMR analysis was conducted to assess the site-specific phosphorylation sites in each phosphorylation state (Fig S3). Additional mutations were introduced for Site Directed Spin Labeling (SDSL) Electron Paramagnetic Resonance (EPR) experiments as the technique requires the introduction of Cysteine used as target for nitroxide spin labels. Two single cysteine variants of Tau AT8 mutant (variant 1: S185C C291A C322A and variant 2: A227C C291A C322A) were produced as described above and phosphorylated at p-state 1 and 2 prior to spin labeling (Fig 1).

NMR spectroscopy

Sample preparation

For NMR experiments, samples of ^{15}N, ^{13}C-labeled Tau AT8 (400 µM), and its phosphorylated variants p-state 1 and p-state 2 were prepared in 300 µL of 25 mM phosphate buffer pH 6.4, 50 mM NaCl, 2.5 mM EDTA, 2 mM TCEP in 95% H2O/5% D2O. For chemical shift referencing, 1 mM sodium 3-trimethylsilyl-3,3′,2,2′-d4-propionate was added to the sample and served as the ^{1}H reference, with ^{15}N and ^{13}C chemical shifts indirectly referenced based on ^{1}H chemical shifts.

Data acquisition and processing

5 mm-NMR Shigemi tubes were filled with tau samples for acquisition of 2D ^{1}H-^{15}N HSQC and 3D experiments at 293 K using a 900 MHz Bruker Avance spectrometer equipped with a triple- resonance cryogenic probe head. Classical backbone assignment was performed on the non-phosphorylated Tau AT8 mutant using various 3D experiments, including HNCACB, HNCO, HNcaCO, HncaNNH, and hNcaNNH, with additional n-CaCON and NCO experiments for proline assignment. All 3D

spectra were acquired using non-uniform sampling. Data acquisition and processing were carried out using Bruker Topspin 4.4.0. Following this, NMRFAM-Sparky was employed for NMR data analysis, and the results were cross-validated using the I-PINE web server. The assignment of phosphorylation sites in p-state 1 and p-state 2 Tau AT8 samples has been made through HNCACB and hNcaNNH experiments.

Determination of WT Tau and Tau AT8 proteins concentration

Lyophilized WT Tau, Tau AT8 mutants and their phosphorylated p-state 1 and p-state 2 forms were resuspended in 20 mM NaPi pH 6.5 buffer containing 1 mM TCEP. Following centrifugation for 10 min at 1500*x g*, the supernatant was diluted to an appropriate concentration for UV-Visible spectroscopy. The absorbance spectra were recorded from 250 to 600 nm using a JASCO-V750 spectrophotometer. To account for light scattering, a mathematical model was employed to correct the absorbance values ($y=a+bxe^{-c}$), where y is the corrected absorbance value, x the measured absorbance value and a, b, and c the fitting constants. Tau concentration was determined using an extinction coefficient of 7700 $M^{-1}.cm^{-1}$ at 280 nm with an optical density (OD) between 0.4 and 0.6.

Protein spin labeling and EPR spectroscopy

Spin labeling variants (positions 185 and 227) of Tau and phosphorylated Tau (p-state 1 and 2) and further continuous wave (cw) EPR analyses were performed as described in [18]. In brief, cysteine reduction was first done by incubating the variants with TCEP (20 mM final, 30 min in ice bath). After removal of TCEP by gel

filtration (PD-10 column, *GE Healthcare*, elution buffer 20 mM NaPi pH 6.5), the nitroxide spin label MTSL ([1-oxyl-2,2,5,5-tetramethyl-δ3-pyrroline-3-methyl] methanethiosulfonate; *TRC Inc.*, Toronto, Canada) was added to the sample (10 molar excess, 1 hour in ice bath). Unreacted spin labels were removed by a desalting column PD-10. Cw-EPR spectra were recorded on an Elexsys 500 Bruker spectrometer at X-band (Super High Q sensitivity resonator) using a Bruker N_2 temperature controller (Bruker ER4131VT). Acquisition parameters were 10mW for microwave power, 0.1 mT and 100 kHz for magnetic field modulation amplitude and frequency respectively.

Hydrodynamic radius determination by Dynamic Light Scattering (DLS)

Dynamic Light Scattering (DLS) with Malvern Zetasizer Pro equipment was employed to investigate the size distribution and hydrodynamic radius (Rh) of WT Tau, unphosphorylated AT8 mutant and in its phosphorylated p-state 1 and p-state 2 forms. Samples were prepared in a 20 mM NaPi buffer pH 6.5 with 1 mM TCEP and analyzed at 20°C at different protein concentrations (between 0.045 and 1.83 mg/mL). The solvent refractive index and viscosity were set to 1.33 and 1.002 mPa.s, respectively. Data were collected using the Hückel approximation, for triplicates with 150 measurements per sample. The hydrodynamic radius of the particles was determined using the Stokes-Einstein equation: $Rh = k_B T/(6\pi\eta D)$, where Rh is the hydrodynamic radius, k_B is the Boltzmann constant, T is the temperature (in K), η is the viscosity of the solvent (in Pa.s), and D is the diffusion coefficient (in $m^2.s^{-1}$). The diffusion coefficient was calculated from the measured relaxation time (τ) using the

following relationship: $\tau = 1/(q^2 D)$, where q is the scattering vector.

To determine the distribution of particle sizes, the data were analyzed using two methods: The Hydrodynamic Volume Analysis, providing information about the relative abundance of particles with different sizes; and the Scattered Light Intensity Analysis, providing a more accurate determination of the hydrodynamic radius of the dominant species in the sample.

Hydrodynamic radius determination by Analytical UltraCentrifugation (AUC)

Sedimentation velocity experiments for WT Tau, Tau AT8 mutants and its phosphorylated p-state 1 and p-state 2 forms were carried out on a Beckman Optima Analytical UltraCentrifuge equipped with absorbance optics. Samples were centrifuged at 60 000 rpm at 20°C into 12 mm double-sector aluminum centerpieces. The absorbance scans were acquired at 275 nm. The raw data were analyzed using the C(S) method implemented in the **SEDFIT** software[20], which fits the sedimentation profiles to a continuous distribution of sedimentation coefficients. This model accounts for diffusion and provides high-resolution separation of species based on their hydrodynamic properties. The C(S) distribution provides the sedimentation coefficient of each species and their relative concentration. To account for the effects of temperature and solvent viscosity, these coefficients were corrected to standard conditions (20°C, in water) using the SEDNTERP software [21]. The partial specific volume of WT Tau and Tau mutant was calculated to be 0.736 mL/g and 0.729 mL/g respectively (SEDNTERP software).

The solvent density and viscosity were found to be 1.0029 g/mL and 0,01002 poise,

respectively. The hydrodynamic radius was obtained using the definition of the sedimentation coefficient and the following Svedberg equation : $Rh = M(1 - \bar{\upsilon}\rho) / (6\pi\eta N_a S)$. Where M is the molecular mass, $\bar{\upsilon}$ is the partial specific volume, ρ is the solvent density, η is the viscosity of the solvent, N_a the Avogadro's number and S the sedimentation coefficient.

Statistics

Linear regressions were performed using the free software Jamovi [The jamovi project (2024). *jamovi*. (Version 2.6). Retrieved from https://www.jamovi.org].

To compare the different forms of Tau, we analyze the variations in their hydrodynamic radii and sedimentation coefficients in function of Tau concentration by linear regression. Their confidence intervals were determined as described below. We first determined the variance of the intercept of the linear regression b obtained both in DLS and sedimentation velocity experiments with equation :

$$S_b^2 = S_y^2(1 - r^2) \sum x_i^2 / (S_x^2 n(n - 2)) .$$

S_b^2 is the variance of the intercept b; S_y^2 is the variance of the y (apparent Rh or sedimentation coefficient $S_{app,20,W}$); S_x^2 is the variance of the x (the concentration); r^2 is the coefficient of determination of the linear regression and n the number of points.

Then, the confidence interval was calculated using equation (3): $b \pm t_{n-2,\alpha}\sqrt{S_b^2}$. Where t is the student parameter obtained for the $n - 2$ degree of freedom and α is the risk $(= 0.05)$ with the Bonferroni correction.

Molecular dynamics simulations: pCALVADOS implementation

The second version of CALVADOS was released in 2022 with improvements regarding dependency on temperature and salt concentration [22] and was recently used on a large-scale study of the Intrinsically Disordered Regions (IDRs) of nearly all the human proteome [23]. Its capacity to generate protein conformational ensembles at low computational cost and its easy implementation in a Google Colab (https://github.com/KULL-Centre/_2023_Tesei_IDRome/blob/main/IDRLab.ipynb) makes CALVADOS a valuable tool to study long IDPs such as Tau. Moreover, since its training set contains the Tau protein and since it has already been used successfully to predict hydrodynamic radii values by Pesce et al. [24], we deemed it a reliable forcefield to use as a base for our study.

We thus performed MD simulations in order to obtain Conformational Ensembles (CoEs) of Tau wild-type and the phosphorylated and unphosphorylated AT8 mutants. At time of writing, CALVADOS did not yet include parameters for phospho-residues, now made available by Rauh et al [13]. We therefore extracted them from the model by Perdikari et al which is also an HPS- based model [14]. This led to the creation of a new parameter set named pCALVADOS, by merging the parameters of CALVADOS 2 [22] with those of doubly charged phosphoserine, phosphothreonine, and phosphotyrosine described by Perdikari *et al* (Table S1 in [14]). Since this kind of “mix-and-match” approach regarding parameters of phospho-residues has proven successful in the past for all-atom force fields, we assumed it might also be the case for coarse-grain approaches, as long as the base model is the same. This assumption was shown to be correct in another work [25], in which a direct

comparison with the parameters by Rauh et al showed highly similar dynamic behaviors at global and local scales.

The pCALVADOS parameter set is provided in the following CSV file: https://github.com/Jules-Marien/Articles/blob/main/_2025_Lohberger_Marien_pCALVADOS/pCALVADOS/pCALVADOS_residues_and_phosphoresidues.csv.

Phosphoresidues were named based on the Amber nomenclature for the 3-letter denomination and were each given an arbitrary letter as a 1-letter denomination (SEP = B, TPO = J, PTR = O). One simply needs to replace S, T or Y in the sequence by their phospho-residue 1-letter equivalent in order to launch a simulation with phosphorylations. The IDRLab Jupyter Notebook designed by Tesei et al was modified to account for pCALVADOS and to run our simulations of all mutants and p-states.

(IDRLab:https://github.com/KULL-Centre/_2023_Tesei_IDRome/blob/main/IDRLab.ipynb). We used OpenMMv7.7 as the simulation engine and simulations were performed in the NVT ensemble with a timestep of 10fs and a Langevin integrator with a 0.01ps^{-1} friction coefficient. The temperature was set at 300K and ionic strength to 0.02 mol.L^{-1} to match the DLS experiment. Termini were charged and histidines were kept neutral. Trajectories were run for 100100000 steps, a simulation length sufficient to ensure convergence for an IDP of the length of Tau according to previous studies [22,23]. We also directly tested convergence of global and local observables and showed that it was indeed achieved (see discussion in the Supplementaries, Fig S4 and S7). The 100000 first steps were discarded as equilibration since the protein chain starts as a straight string of beads. Frames were then sampled every 5000 steps, providing a CoE of 20000 evenly-spaced frames.

From coarse-grain to all-atom

pCALVADOS, as a coarse-grained forcefield, represents each residue as a single bead. It could however be interesting to recover some of the information provided by sidechains, especially as we are interested in phosphorylation. Tesei et al. already proposed a protocol based on the PULCHRA program to convert a CALVADOS trajectory to an all-atom trajectory [26]. PULCHRA is, however, not capable of converting phospho-residues to all-atom representation, and simply provides canonical residues instead. We therefore designed a new protocol to recover all-atom trajectories. Scripts are available at https://github.com/Jules-Marien/Articles/tree/main/_2025_Lohberger_Marien_pCALVADOS/Scripts_CG_2_AA.

At first, PULCHRA was used to generate unphosphorylated all-atom trajectories. A TCL script was then used in combination with VMD to add the proper phosphorylations using CHARMM patches [26] and generate a topology file per conformation. A minimization of 100 steps was performed on each resulting frame using NAMD and the CHARMM36m forcefield, constraining only the backbone heavy atoms to preserve the overall conformation [27,28]. This step allows on one hand to relax any steric and electrostatic tensions induced by adding phosphorylations and also provides a better extrapolation of the sidechains thanks to a state-of-the-art all-atom force field. The relaxed conformations were then re-assembled into an all-atom phosphorylated trajectory. The same protocol was followed for unphosphorylated systems for consistency. Both raw coarse-grain trajectories and relaxed all-atom trajectories are available on Zenodo: https://doi.org/10.5281/zenodo.14900596.

Rh simulation analysis and new metrics

All analyses were performed using Python scripts based on the MDAnalysis and MDTraj packages [29,30]. Hydrodynamic radii were calculated using the Nygaard method [https://www.sciencedirect.com/science/article/pii/S0006349517306926] as described by Pesce et al. [24], inspiring ourselves from the following scripts: https://github.com/KULL-Centre/papers/tree/main/2022/rh-fwd-model-pesce-et-al/Rh_scripts. The linear fit of experimental Rh was performed with the curve fit function of the scipy.optimize module [31].

Contact maps were computed by defining a contact as two heavy atoms from two different residues within 5 Å of one another, then calculating the percentage of simulation time during which a pair of residues is in contact. Proteic Menger Curvatures (PMCs), Local Curvatures (LCs) and Local Flexibilities (LFs) were calculated using the previously published Python module [15] :

https://github.com/Jules-Marien/Articles/blob/main/_2024_Marien_nPcollabs/Demo_and_scripts_Proteic_Menger_Curvature/MODULE_Proteic_Menger_Curvature.py.

LFs have been shown to correlate significantly with the translational relaxation time T2 for the Tau protein, making the metric a valuable probe of the dynamics of the backbone [25].

Convergence of the simulations is discussed in the Supplementary materials.

Results

Characterization of phosphorylated and unphosphorylated AT8 mutants

To study the specific effects of Tau phosphorylation at the AT8 epitope, a Tau protein mutant was created with 16 phosphorylation sites specific of CDK2/cyclinA and GSK3β kinases mutated into Alanine except those recognized by the AT8 antibody (Figs 1 and S1). The mutant is then turned into two different phosphorylation states using distinct kinase combinations. p-state 1 is achieved by incubating the Tau mutant with CDK2/cyclin A kinase, and p-state 2 by incubating the Tau mutant in p-state 1 with GSK3β kinase. The overall phosphorylation levels are estimated by SDS-PAGE and MALDI-TOF mass spectrometry (Fig S1) while the site-specific phosphorylation patterns are determined using high-resolution NMR spectroscopy. Given the high sensitivity of the N-H amide resonances to modifications of their chemical environment such as phosphorylation events, chemical shift perturbations are detected in the ^{1}H-^{15}N HSQC spectra for Ser/Thr phosphorylation sites and neighboring residues (Fig 2). In IDPs, Ser/Thr phosphorylation induces a large perturbation of the resonances which appear in an empty region of the IDP's ^{1}H-^{15}N HSQC spectrum. In addition, by integrating the respective amide resonances of the phosphorylated and non-phosphorylated forms of a given Ser/Thr residue, levels of phosphorylation can be measured in a site-specific manner.

The 2D ^{1}H-^{15}N HSQC spectrum of the Tau AT8 mutant in its non-phosphorylated state has been assigned using a set of three-dimensional backbone assignment experiments. Additional 3D NMR experiments on both phosphorylated Tau AT8 mutants enabled the assignment of resonances for p-state 1 and p-state 2 that have been shifted upon phosphorylation. By interpreting the NMR spectra of the Tau mutant in its non-phosphorylated or phosphorylated states, in combination with mass spectrometry analyses (Figs S2 and S3), we concluded that p-state 1 results in the full phosphorylation of Serine at positions 202 and Threonine at position 205 and

212, as evidenced by the detection of new resonances at higher chemical shifts that have been assigned to the phosphorylated forms of those residues, together with the disappearance of the corresponding resonances in the non-phosphorylated state (Figs 2 and S3). The effect of phosphorylation is also observed for residues in close proximity to the phosphorylation sites such as S208 and S198, whose resonances shift upon phosphorylation of S202, T205 and T212. In addition, we observed a marked shift for G207 resonance in p-state 1, that has been linked to the formation of a local *β*-turn conformation upon double phosphorylation of S202 and T205 [8,9]. We observed in p-state 2 two additional phosphorylation sites on Serines 198 and 208 each at a phosphorylation level close to 100% (Figs 2 and S3). In contrast to the double phosphorylation of S202 and T205 in p-state 1, triple phosphorylation of AT8 at S202, T205 and S208 in p-state 2 induces a limited shift of G207 resonance (as compared to the non-phosphorylated state) which was suggested to disrupt the local *β*-turn conformation of p-state 1, probably restoring an extended conformation in this region [9]. By creating these two distinct phosphorylation states, we can investigate the effects of different phosphorylation patterns within the AT8 epitope without interference from other phosphorylation events.

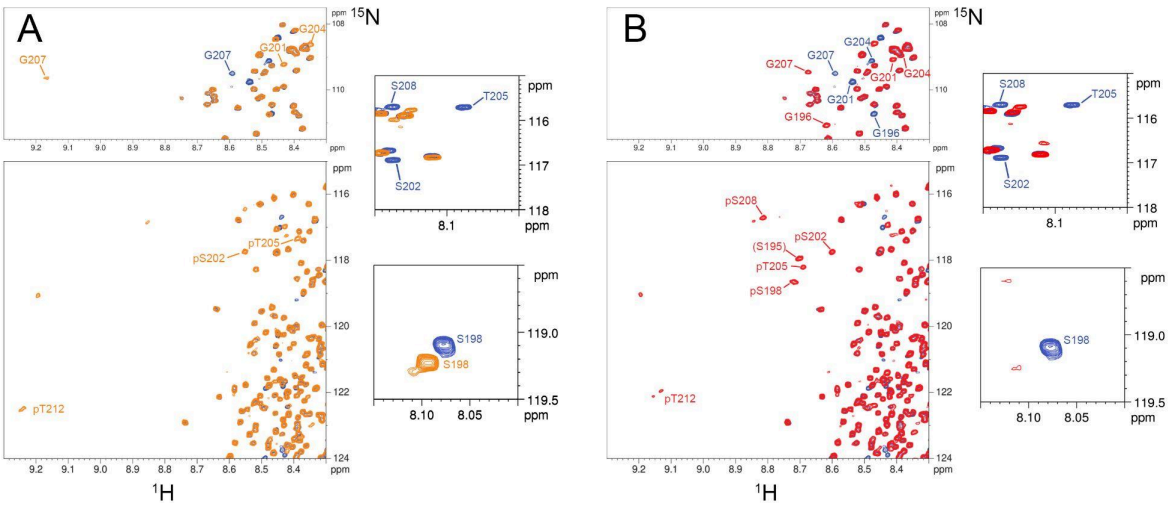

Fig 2: Expanded views of NMR ^{1}H-^{15}N HSQC spectra of the unphosphorylated AT8 mutant (blue), the mutant in p-state 1 (orange) and in p-state 2 (red), highlighting the site-specific phosphorylation sites in each phosphorylation state. (A) Comparison of the spectra of the mutant in p-state 1 and the unphosphorylated state. (B) Comparison of the spectra of the mutant in p-state 2 and the unphosphorylated state. The regions of phosphorylated Ser/Thr and Gly (left panels) are depicted to show the chemical shift perturbations of resonances upon phosphorylation. S202/T205 double phosphorylation in p-state 1 and S202/T205/S208 triple phosphorylation in p-state 2 have a differential impact on G207 resonance which is found in the center of the AT8 motif. The unphosphorylated S202, T205, S208 and S198 resonances are depicted (right panels) to show their disappearance or shift upon phosphorylation.

Determination of the hydrodynamic radius by different methods

To investigate the hydrodynamic properties of Tau and of the unphosphorylated and phosphorylated AT8 mutants, we performed Dynamic Light Scattering (DLS) and Analytical UltraCentrifugation (AUC) measurements. In DLS experiments, correlograms show a typical decay pattern expected for a diffusing species (Fig S5). The correlation coefficient starts high (0.9), indicating strong initial correlation, and decays smoothly towards zero as time increases. This decay is consistent with Brownian motion of particles in solution and high quality of the provided data. Although DLS is primarily used for globular proteins, it can still provide information about conformational ensembles in IDPs and especially aggregation states. The volume-weighted distribution was used to estimate the percentage of protein present

at a given hydrodynamic radius. Even if no other peaks were present on the volume-weighted distribution graph (Fig S5), our samples Polydispersity indexes (PI) are between 0.5 and 0.6 for WT Tau, 0.4 and 0.7 for the unphosphorylated AT8 mutant, 0.2 and 0.6 for p-state 1 and 0.2 and 0.7 for p-state 2 (PI =0 for a monodisperse sample and PI=1 for a polydisperse sample) which indicates a relative variability in the polydispersity. Because Tau protein is well known for its capacity to aggregate, this polydispersity could be explained by aggregation that slows down the diffusion coefficient resulting in an apparent larger Rh. By consequence, the hydrodynamic radius is obtained by plotting the measured hydrodynamic radius as a function of protein concentrations and extrapolating with a linear regression to infinite dilution (Fig 3, Fig S6). WT Tau exhibited a Rh of 4.9 nm with a confidence interval of 0.8 nm in agreement with this obtained previously [32,33]. The unphosphorylated AT8 mutant displayed the same value of Rh of 5.0 ± 1.2 nm. The observation that the mutant exhibits a hydrodynamic radius comparable to that of wild-type Tau suggests that this mutant provides a suitable model for investigating AT8-specific phosphorylation. The p-state 1 has a Rh value of 5.8 ± 1.2 nm and the p-state 2 displays a Rh of 5.0 ± 0.6 nm. The confidence intervals obtained for the four different samples overlap, indicating no statistical significant difference in the hydrodynamic radii. By consequence, the phosphorylation state of AT8 Tau mutant has no effect on the global shape of this protein. On the other hand, the positive slope of the linear regression indicates an increase of Rh as a function of the concentration that represents the aggregation tendency of the sample in agreement with the polydispersity index. This tendency is strong for both the unphosphorylated AT8 mutant (Fig 3B) and the p-state 2 (Fig 3D). In contrast, WT Tau (Fig 3A) and the p-state 1 phosphorylated mutant (Fig 3C) exhibit a much lower concentration

dependence. However, it is important to note that a low slope in DLS does not preclude the presence of stable oligomers, as a distinct population of such species was detected for p-state 1 by AUC (see below, Fig 4C).

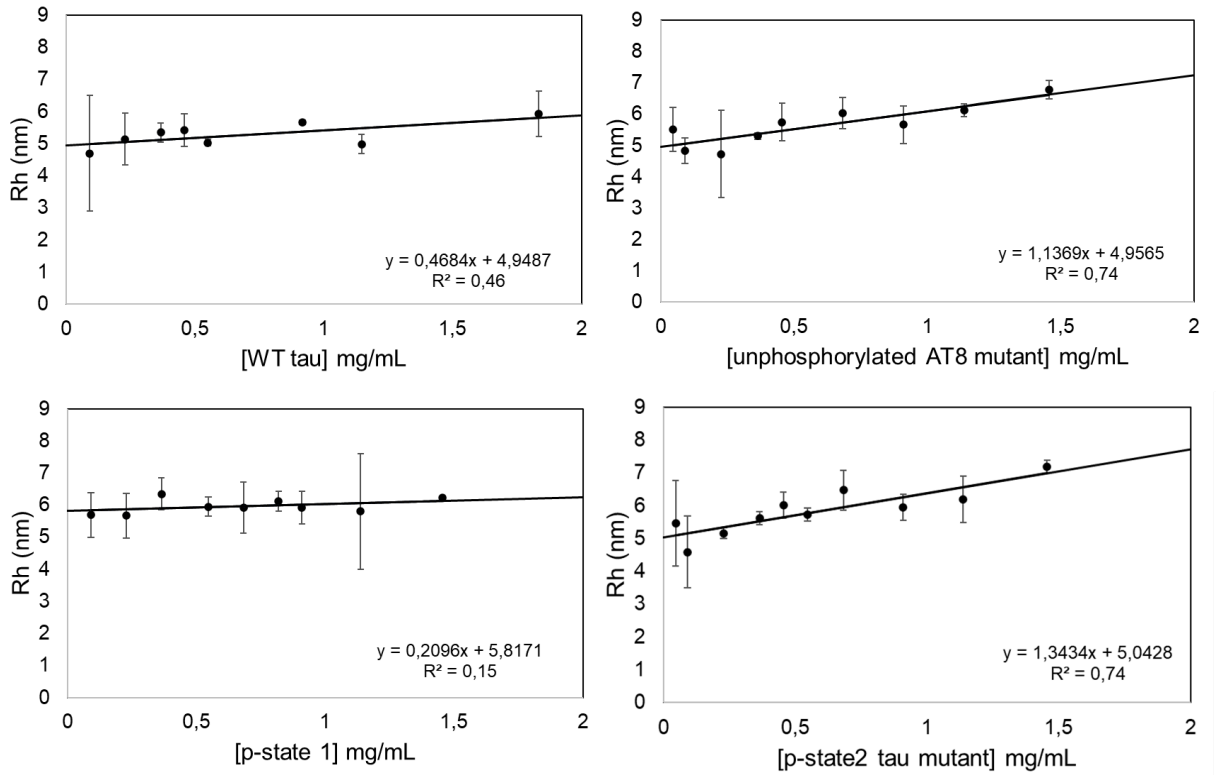

Fig 3: Hydrodynamic radius of WT Tau, unphosphorylated AT8 mutant, p-state 1 mutant and p-state 2 mutant as a function of protein concentration. Apparent Rh measured from DLS experiments and the linear regression in black. (A) Wild-type Tau (concentration range 0.09-1.83 mg/mL). (B) unphosphorylated AT8 mutant (concentration range 0.045-1.45 mg/mL). (C) Tau mutant in p-state 1 (pS202 + pT205 + pT212) (concentration range 0.09-1.45 mg/mL). (D) Tau mutant in p-state 2 (pS198 + pS202 + pT205 + pS208 + pT212) (concentration range 0.045-1.45 mg/mL). The error bars indicate the standard deviation of the average Rh value obtained from a triplicate.

A second experimental approach was employed to confirm the absence of impact of

phosphorylation on the global conformation of Tau. The sedimentation velocity experiment in Analytical UltraCentrifuge is a highly reproducible and quantitative method that allows the determination of the sedimentation coefficient (S). This parameter reflects both the molecular mass and the hydrodynamic shape of the protein. The displacement of the protein by the centrifuge force, measured by changes in absorbance as a function of the centrifugation radius over time, is analyzed as a distribution in which each peak corresponds to a different molecular species with a distinct sedimentation coefficient.

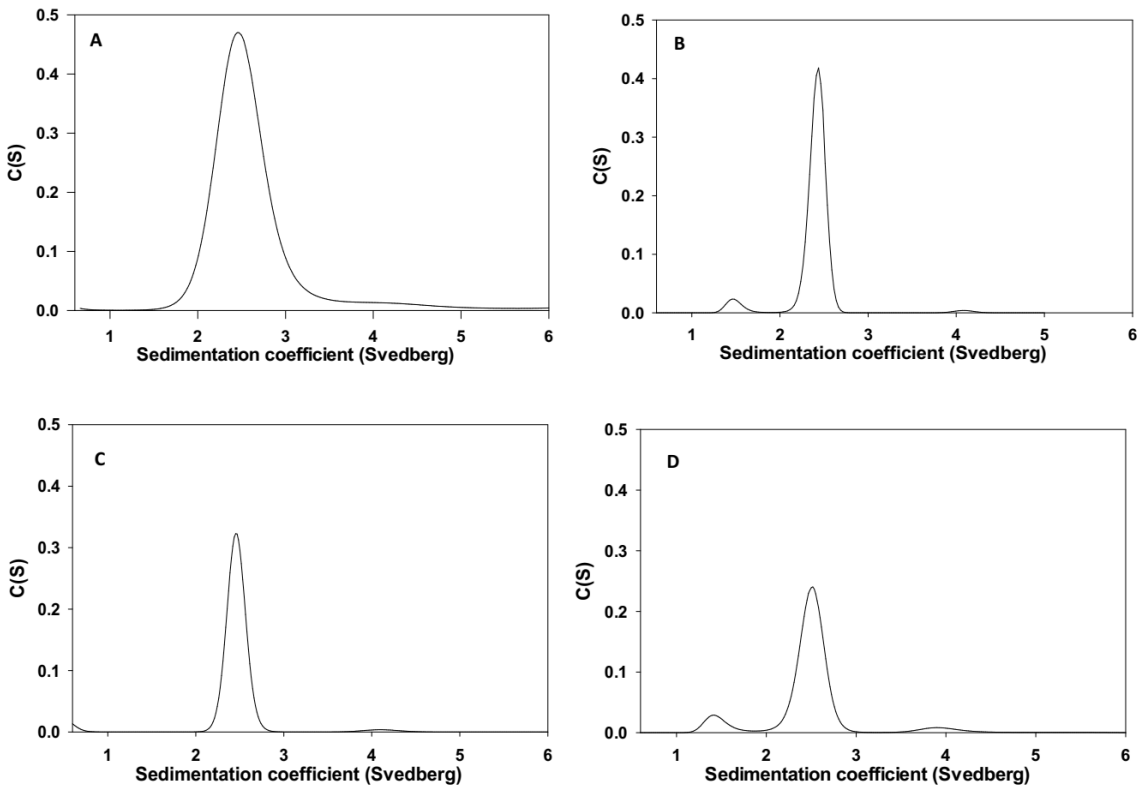

Fig 4: Analytical sedimentation velocity experiment analysis of WT Tau and its AT8 mutant unphosphorylated and phosphorylated in p-state 1 and 2. Sedimentation coefficient distribution determined by Sedfit analysis of 1.25 mg/mL of WT Tau **(A)**, of 0.46 mg/mL of unphosphorylated AT8 mutant **(B)**, of 0.43 mg/mL of AT8 mutant in p-state 1 **(C)** and of 0.35 mg/mL of AT8 mutant in p-state 2 (D).

Sedimentation coefficient distribution determined by Sedfit analysis.

For WT Tau, the C(S) distribution shows a major peak at 2.5 ± 0.6 Svedberg (S), corresponding to the monomeric form of Tau (Fig 4A). A shoulder observed around 4 S suggests the presence of a small amount of Tau oligomers or aggregates. In the case of the unphosphorylated AT8 mutant (Fig. 4B), the main peak corresponding to monomeric Tau is centered at 2.4 ± 0.1 S. This peak appears sharper and narrower compared to that of WT Tau, suggesting a reduced conformational variability within the sample. Additionally, a smaller peak appears at 1.5 ± 0.1 S, which may correspond to degradation products or truncated Tau species. For the AT8 mutant in p-state 1 (Fig. 4C), the C(S) distribution displays two peaks: one corresponding to the monomeric Tau, and another at higher S-value (approximatively 4S) corresponding to a small amount of aggregated species. Notably, no degradation peak is detected under these conditions. Finally, the AT8 mutant in p-state 2 (Fig. 4D) exhibits three peaks in the C(S) distribution: one corresponding to the monomer (2.4 ± 0.3 S), a second reflecting aggregation at (approximately 4S), and a third consistent with a degradation product at approximately 1.5 S, like the unphosphorylated form. Due to hydrodynamic non-ideality, which increases intermolecular friction through crowding effects, the apparent sedimentation coefficient of the monomer peak of each sample was measured, plotted for various Tau concentrations, and analyzed by linear regression. This analysis yielded the standard sedimentation coefficient at infinite dilution ($S^0_{W,20}$) representing the intrinsic sedimentation behavior of the molecule in the absence of interparticle interactions (Fig 5). We obtained a sedimentation coefficient of 2.4 ± 0.3 S, 2.4 ± 0.3 S, 2.2 ± 0.3 S and 2.4 ± 0.3 S for WT Tau

monomer, unphosphorylated AT8 mutant, mutant in p-state 1 and p-state 2 respectively. The confidence intervals overlapped for the four different Tau monomers indicating no significant difference in the sedimentation coefficients. This points towards a lack of effect of the mutations and of the phosphorylation state of Tau in monomeric state.

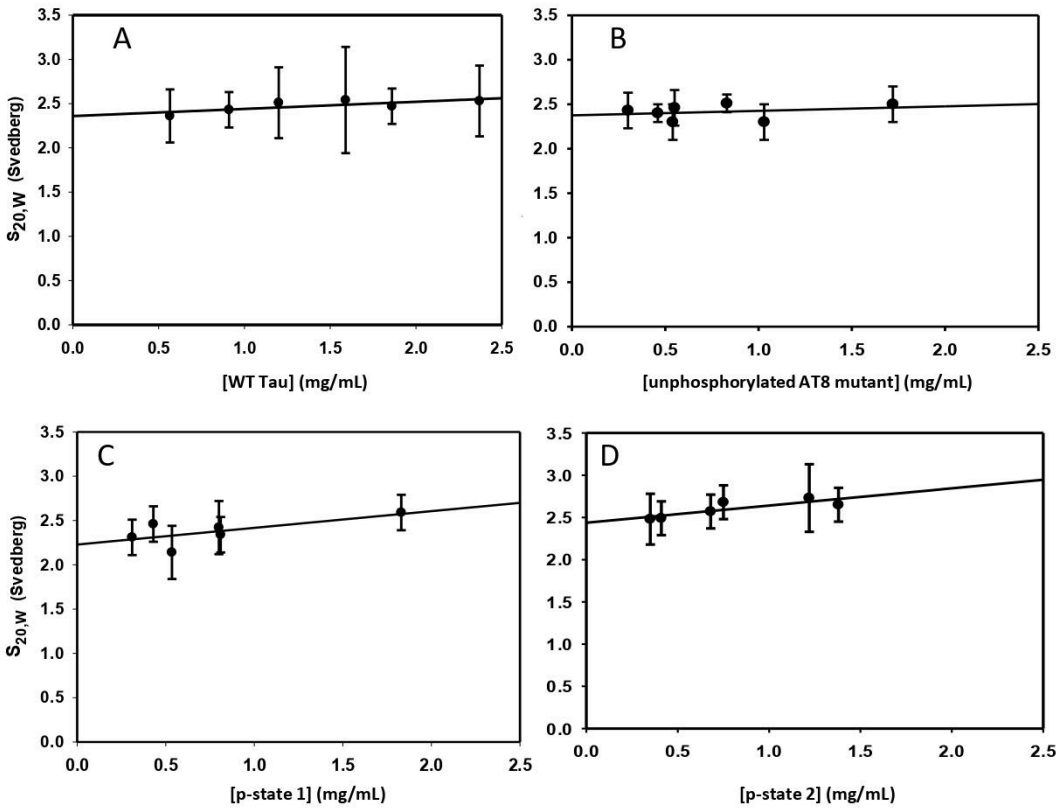

Fig 5: Determination of standard sedimentation coefficient by AUC. The apparent sedimentation coefficients (S_{app}) of WT tau **(A)**, unphosphorylated AT8 tau mutant **(B),** and its p-state 1 **(C)** and p-state 2 **(D)** phosphorylated form determined from figure 4 at several concentrations using analytical ultracentrifugation sedimentation velocity experiments. Each S_{app} was corrected to standard conditions (20°C, water as solvent) to yield $S_{app,20,W}$ values. These values were plotted against concentration, and a linear fit was applied to account for concentration-dependent

effects due to hydrodynamic non-ideality. The extrapolation of this fit to infinite dilution yields the standard sedimentation coefficient, $S^0_{app,20,W}$, representing the intrinsic sedimentation behavior of the molecule in the absence of interparticle interactions.

Values of hydrodynamic radii were estimated from the sedimentation coefficient with the Svedberg equation (see Materials and methods). The obtained values are in accordance with those measured directly by DLS and confirm the absence of effect of the mutations and of phosphorylations on the global conformation of Tau (Table1). Values for the hydrodynamic radius (Rh) were computed using the Nygaard method specifically developed with IDPs in mind. According to Pesce et al, this method is highly suitable for determining the Rh of Tau [32]. Consistent with this, we obtained a computed Rh value of 5.2 +/- 0.7 nm. The hydrodynamic radii obtained using both experimental and computed methods are consistent within this study and others [32], suggesting a good reliability of the results (table 1).

Protein	DLS experimental Rh	AUC experimental Rh	Nygaard method Rh
WT Tau	4.9 ± 1.3 nm	4.5 ± 0.6 nm	5.2 ± 0.7 nm
unphosphorylated AT8 mutant	5.0 ± 1.2 nm	4.5 ± 0.6 nm	5.2 ± 0.7 nm
AT8 Tau mutant p-state 1 (pS202, pT205, pT212)	5.8 ± 1.2 nm	4.6 ± 0.6 nm	5.1 ± 0.7 nm
AT8 Tau mutant p-state 2 (pS198,	5.0 ± 1.8 nm	4.5 ± 0.6 nm	5.1 ± 0.7 nm

pS202, pT205, pS208, pT212)			

Table 1: Hydrodynamic radius of wild-type and phosphorylated Tau variants as determined by, DLS, and AUC experiments and pCALVADOS simulations.

Local dynamics

DLS and AUC experiments revealed no significant differences between p-states in the global dynamics of Tau. We therefore asked whether a change could be observed in the local dynamics, at the residue scale. The transient nature of intramolecular interactions can be investigated via the simulated trajectories using contact maps derived from the simulated CoEs (Figs S7, S8 and S9 and Materials and Methods). All contacts made between two residues in all systems are present less than 10% of the simulated time, indicating a very dynamic behavior of the peptide chain (Fig S8). To assess the local impact of the mutations and of the phosphorylations, we decided to use the wild-type Tau simulation as a reference. We subtracted the contact map of the wild-type to the mutant and its different p-states to highlight which contacts are impacted. Fig 6A displays the difference between the unphosphorylated AT8 mutant and Tau wild type. Long-range interactions are barely modified by the alanine mutations with differences compared to reference of less than 1%, and local interactions (within five residues) mostly show negligible losses of contacts inferior to 5%. The comparison with the phosphorylated states, however, reveals interesting local and long-range effects. Contacts are strengthened within 50 residues of the epitope, notably with R170, K174, K190 and R194 on the N-terminal side and with R221, K224, K225, R230, K234, K240 and R242 on the C-terminal side (Figs 6B and

6C). On the other hand, and quite surprisingly, contacts are weakened at very long residue-range (up to 200 amino-acids away) when the epitope is phosphorylated, with a stronger effect on residues E53, D54, E55, E57, E58 and a weaker one for D34, E35, E38, E73, E104 and E105. The effect is also only present for the N-terminal part of Tau, which indicates that the unphosphorylated epitope has a preferential affinity with it. These contact differences also increased as the number of phospho-residues increased, suggesting that they are of electrostatic nature.

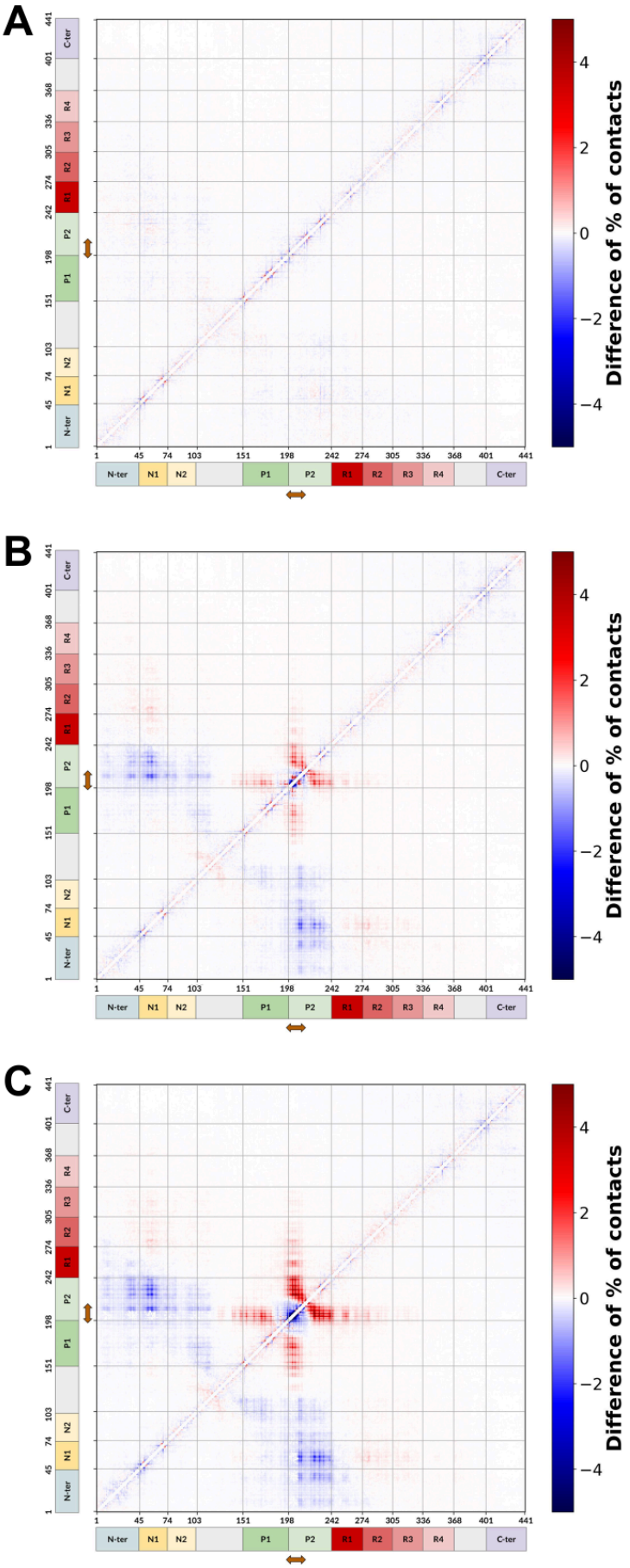
A
B
C
N-ter
N1
N2
P1
P2
R1
R2
R3
R4
C-ter
1
45
74
103
151
198
242
274
305
336
368
401
441
Difference of % of contacts
4
2
0
−2
−4

Fig 6: Difference of percentages of contacts per residue pairs between the Tau wild type unphosphorylated and the AT8 mutant (A), the mutant in p-state 1 (B), the mutant in p-state 2 (C) . Contact gains are in red, contact losses are in blue. The AT8 epitope is indicated by a brown arrow.

Local curvatures and flexibilities

In order to decipher changes in backbone dynamics, we employed computational metrics specifically designed to make sense of the backbone CoE of IDPs without the need for alignments or reference structures. The Local Curvatures (LCs) and Local Flexibilities (LFs), derived from the Proteic Menger Curvatures (PMCs) distributions of the residues, can assess the average curvature of the backbone and its fluctuations [16]. We previously introduced these metrics to characterize bending of the protein backbone induced by counterion bridges in multi-phosphorylated peptides [15]. Hence, we once again used the Tau wild-type simulation as a reference to assess the effects of the mutations and phosphorylations on the local curvature and flexibility of the backbone. The lack of significant differences in LCs and LFs at the substitution sites (Fig S7 and S9) confirms that the Tau mutant serves as an accurate structural surrogate. This validates our model, ensuring that observed changes are attributable to phosphorylation rather than the mutations themselves. Notably, phosphorylation triggers a pronounced effect on backbone dynamics spanning residues 195 to 215 (Fig 7). Local stiffening and elongation of the backbone, probably due to electrostatic repulsion from the addition of multiple phosphorylations, is observed, as both the curvature and the flexibility of the epitope residues are reduced. This effect depends on the number of phosphorylation as LCs are only decreased by -0.025 $Å^{-1}$ for P203 and G204 for p-state 1, whereas most residues

from A199 to P206 see their LC drop by more than -0.025 $Å^{-1}$ for p-state 2 (Fig 7A). The difference between p-states is even more noticeable with LFs as differences with the wild-type for P200 and S210 are three times higher for p-state 2 than for p-state 1 (Fig 7B).

Spin-labeling combined with EPR spectroscopy was used to experimentally assess the local flexibility at two specific positions (185 and 227) where single cysteine residues were introduced to graft nitroxide spin labels. This technique is very powerful to detect small changes in local flexibility of the protein backbone and particularly sensitive to report local structural changes in IDPs [34,35]. For each position, the EPR spectra showed very narrow lines indicative of high flexibility as expected for an intrinsically disordered region (Fig S10). No significant difference was observed after phosphorylation at p-state 1 and p-state 2. This experimental observation reinforces the findings brought by the calculations of LCs and LFs that showed modifications restricted to the close AT8 region without any fluctuation of these parameters neither downstream nor upstream of this region.

To summarize, pCALVADOS simulations of the backbone dynamics and derived hydrodynamic radii agree with the experimental data. In both cases we demonstrated that there is no effect on the global conformation of Tau. More interestingly, we show a reduction of the curvature and flexibility of the backbone around the AT8 epitope that could hint towards a role of phosphorylation for Tau dynamics.

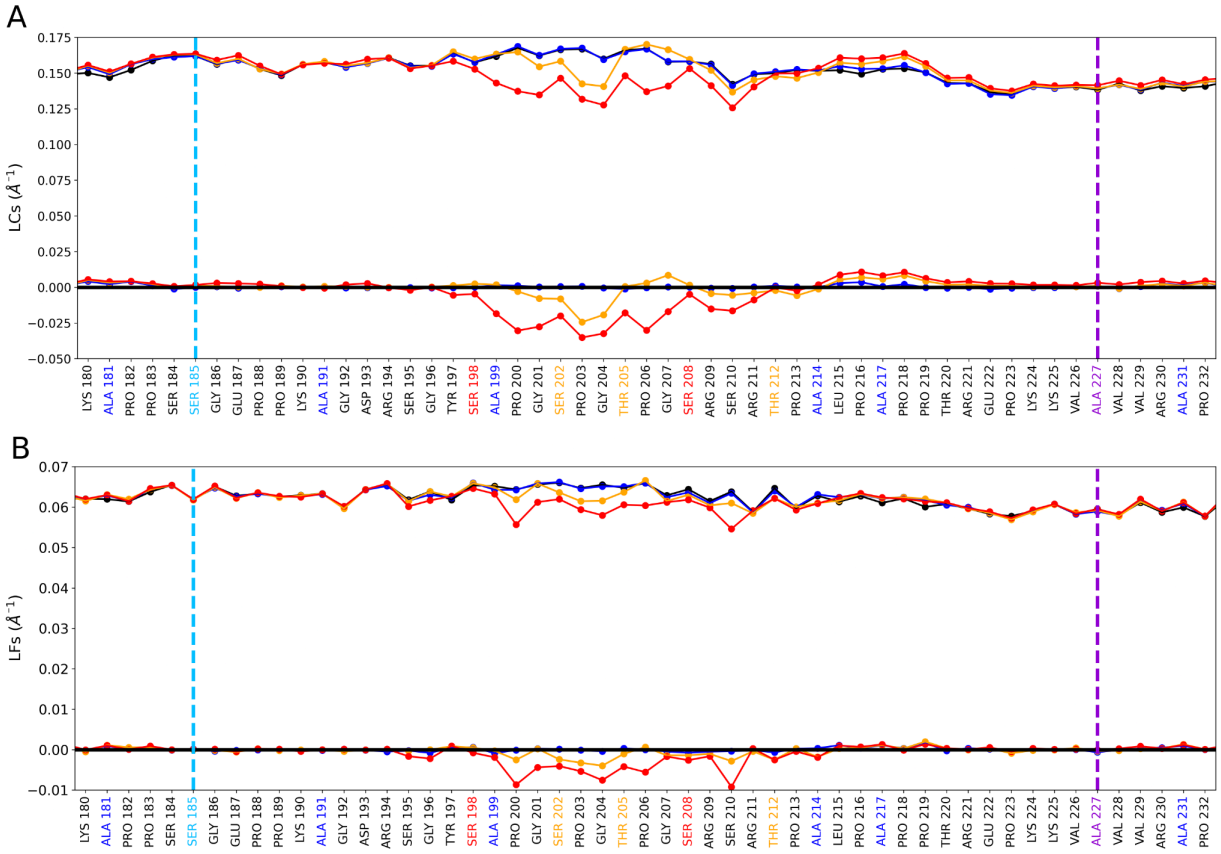

Fig 7: Local Curvatures (A) and Local Flexibilities (B) of the AT8 epitope. Upper curves on each graph represent Local Curvatures (A) and Local Flexibilities (B) for wild-type Tau (black), the unphosphorylated AT8 mutant (blue), the mutant in p-state 1 (orange) and the mutant in p-state 2 (red). The lower curves on each graph represent the difference regarding the wild type. Positive values represent a gain in curvature/flexibility respectively and negative values a loss. Residues in blue have been mutated to alanine compared to Tau wild type. Residues in orange are phosphorylated in p-state 1, residues in red in p-states 1 and 2. The mutated sites used in the EPR experiments for S185C and A227C are indicated in blue and purple dashed lines respectively.

Discussion

Protein phosphorylation is a crucial posttranslational modification catalyzed by kinases which transfer phosphate groups from ATP to specific amino acid residues. This process regulates a wide range of cellular functions, including cell signaling, proliferation, apoptosis, and maintenance of neuronal function [36]. Among these enzymes, the Serine/Threonine kinases constitute an important part of the human kinome, targeting the hydroxyl groups of Serine or Threonine residues. These kinases also phosphorylate the Tau protein, thereby modulating its physiological and pathological roles. In neurodegenerative diseases such as Alzheimer's, the equilibrium between kinases and phosphatases (enzymes that remove phosphorylation) is disrupted, resulting in Tau hyperphosphorylation. Several phosphorylation sites of Tau have been identified as pathological. Among them, phosphorylation at Serine 202, Threonine 205, and Serine 208 defines the AT8 epitope, recognized by a specific antibody routinely employed in the post-mortem diagnosis of Alzheimer's disease [6] and which the intensity staining in brain tissue correlates with the Braak stages that characterize the progression of the disease [7]. The longest isoform of human Tau has 85 potential phosphorylation sites along its 441 amino acid sequence, 40 of which have been characterized experimentally [37,38]. Because understanding their role presents an analytical challenge, previous studies predominantly used phosphorylated Tau peptides, which failed to recapitulate the conformational and functional properties of the complete protein. By consequence in this study, we aimed to restrain the phosphorylation sites within the full-length Tau protein. To achieve this, specific residues previously identified by NMR as phosphorylation sites of CDK2/cyclin A and GSK3β kinases in vitro [8,9] were

substituted with Alanine to prevent phosphorylation [36,37], except for the pathological epitope recognized by the AT8 antibody. Moreover, IDPs, such as Tau, lack a stable 3D structure, making them challenging to study their conformation in solution and giving them significant aggregative properties. We used DLS and AUC to determine the global shape of WT Tau, the unphosphorylated mutant, p-state 1 and p-state 2 through the sedimentation coefficient and the hydrodynamic radius parameters determination. In DLS experiments, we used a range of Tau concentrations and perform a linear regression to determine the Rh at infinite dilution (C=0 M) because IDPs can adopt a wide range of conformations and sizes in solution and have tendency to aggregate, influenced by factors such as protein concentration but also temperature, pH and ionic strength. The Rh of WT Tau obtained by DLS analysis in our study is consistent with values previously reported using the same methodology [39,40]. Interestingly, whereas the Rh of unphosphorylated AT8 mutant and p-state 2 Tau mutant increased linearly with protein concentration (R^2= 0.74 and 0.75 respectively) indicating a propensity to aggregate, it was not the case for WT Tau and p-state1 Tau mutant (R^2= 0.46 and 0.15 respectively). This heterogeneity is confirmed in AUC velocity experiments. Indeed, AUC is a very powerful technique to characterize macromolecules or mixtures of macromolecules in solution by separating them using centrifuge force, allowing the measurement of their hydrodynamic properties: their sedimentation coefficient S [41] and their hydrodynamic radius (see Materials and Methods section). The primary advantage of this method lies in its versatility, as it is applicable to spherical proteins, elongated structures, and IDPs, enabling the identification and quantification of distinct molecular species. Sedimentation velocity experiments analysis applied to WT Tau (Fig 4) shows the presence of one major peak corresponding to monomeric Tau, and

Tau aggregates at higher sedimentation coefficient value confirming the polydispersity of the samples found by DLS. If we consider only the major peak we measured a standard sedimentation coefficient for WT Tau of 2.4 ± 0.1 S and an estimation of the hydrodynamic radius of 4.5 ± 0.8 nm in agreement with our previous work [42]. In this study, we demonstrated that the 16 mutations of serine/ threonine residues into alanine had no impact on the hydrodynamic radius of Tau, irrespective of the experimental methods employed, indicating that the mutant is a suitable model for the study of the two phosphorylation states of Tau. Interestingly, we also found that the two phosphorylation states of AT8 epitope did not modify the Rh of Tau even though its function was described to be modulated by specific phosphorylation patterns [43]. In previous NMR experiments combined with molecular dynamics simulations, Gandhi et al. demonstrated the presence of a kink at residue 207 in pS202/pT205 phosphorylated Tau [8]. The modified Tau protein used in this experiment [8] corresponds to the p-state 1 of the present study. This local conformation was shown to be disrupted by an additional phosphorylation at pS208 corresponding to the p-state 2 phosphorylated Tau [9]. We demonstrated here that these local conformational changes have no effect on the global conformation of Tau. Despres et al. [9] also demonstrated that disruption of the kink in p-state 2 phosphorylated Tau promotes protein aggregation into pathological-like fibers. Despite the different experimental conditions used in the present study (different pH, presence of EGTA and MES buffer instead of phosphate), we similarly observed a stronger aggregation tendency in p-state 2 Tau compared to p-state 1. This observation is particularly visible in AUC experiments, where the area under the peak around 4S corresponding to aggregated species is larger for p-state 2 than for p-state1 (Fig 4 C and D). Overall, our experimental observations highlight that the

global conformational properties of Tau reflected in its hydrodynamic radius remain unchanged upon phosphorylation on AT8 epitope. To further assess whether computational models reproduce this insensitivity of Rh to phosphorylation, we have used the Nygaaard method already applied for unphosphorylated WT Tau protein [24,32]. In their assessment of Rh using the CALVADOS FF, Pesce et al. reported the experimental value of 5.40 +/- 0.20 nm determined by Mukrasch et al. [24,32], However, a re-evaluation of the primary data suggests a value closer to 5.20 +/- 0.20 nm. This adjusted value aligns closely with the linear regression to infinite dilution performed in our study via DLS. Moreover, the experimental flexibility and curvature analysis of Mukrasch et al [32] agree qualitatively with our LCs and LFs for the wild type. We based ourselves on the protocol proposed by Pesce et al. and recovered similar results for the Nygaard Rh despite not using a reweighting technique. This good agreement even with the different p-states tends to confirm the capacity of pCALVADOS to provide relevant Conformational Ensembles for multi-phosphorylated IDPs.

The lack of sensitivity of Rh to mutations, and most importantly to phosphorylations, could be interpreted as a sign that pCALVADOS cannot properly capture the effects of side-chain substitutions due to its coarse-grained nature. Nevertheless the overall agreement of the calculated Rh with the experimental regression to infinite dilution seems to be telling another story. It is possible that phosphorylation effects are more prominent for intermolecular interactions rather than intramolecular ones, which would explain the dependency on concentration observed on Fig 3 and Fig S6. One should however keep in mind the uniqueness problem of CoE, which states that, as bead-like protein models are still complex, there might exist several parameterizations and therefore several CoEs which can fit one target observable

[44]. It is therefore possible that pCALVADOS generates ensembles which fit the experimental Rh but are still not biochemically accurate. To evaluate whether this is the case, we must assess whether our CoE fits other experimental properties of multi phosphorylated IDPs.

Our calculations of LCs and LFs revealed that upon multi phosphorylation, the backbone of the Tau mutant locally adopts a less curved and less flexible dynamics (Fig 7). This behavior was previously observed experimentally by Lasorsa et al. on the same system phosphorylated on pSer202 and pThr205 and could be assessed through the analyses of Paramagnetic Relaxation Enhancement effects and the comparison of the relaxation times of the phosphorylated and unphosphorylated forms [44]. This gives weight to the assumption that the CoEs produced by pCALVADOS well describes the experimental observations. LCs and LFs calculated from the simulations suggest that the impact on the average conformation of the backbone does not propagate further than a few residues from the phosphosites (Fig 7). This aligns well with the lack of difference in cw-EPR signals between the different p-states measured on Fig S10. pCALVADOS simulations could thus be a method of choice to guide the selection of positions for nitroxide spin labels, allowing to check multiple positions and whether they stand within the reach of detectable dynamics modification upon phosphorylation.

It is interesting to note that most experiments are conducted at low salt concentrations, which lack biological relevance. As salt shielding likely impacts the dynamics of multi-phosphorylated Tau in the cell [15], further work is required to mimic the cellular environment. Such investigations could be effectively pursued using Site-Directed Spin Labeling combined with EPR spectroscopy [45] .

Overall, our study constitutes a successful combination of experiments and simulations to study the CoE of a multiphosphorylated IDP at the local and global scales.

Conclusion

Experimental hydrodynamic radius (Rh) measurements from DLS and AUC for WT Tau and the unphosphorylated as well as progressively phosphorylated (p-state 1 to p-state 2) AT8 -phosphorylated mutants were consistent with simulations performed using pCALVADOS 2 forcefield and phospho- residues parameters by Perdikari et al. [14,22]. These findings highlight that specific phosphorylation events at the AT8 epitope do not modulate the hydrodynamic radius and, potentially, the conformational ensemble of Tau.

The generated CoEs display good agreement with experimental Rh using the Nygaard method, as could be expected considering that it is targeted towards IDPs. Our calculations of Local Curvatures and Local Flexibilities confirmed that the mutations on the Tau sequence used to perform selective phosphorylations do not have a significant impact on the local dynamics compared to the wild-type, making the mutant an appropriate surrogate for phosphorylated Tau studies. We also identified a local rigidification and extension of the epitope AT8 proportional to the number of phosphorylation qualitatively supported by several experimental results [32,44]. Long-range effects of phosphorylations were also identified, with an interesting directionality towards the N-terminal end of the Tau protein.

The generation and characterization of the AT8 Tau mutants have laid the groundwork for future studies aimed at elucidating the structure-function relationship of Tau bound on the microtubule. This validated protein will serve as a crucial tool for subsequent studies aimed at establishing a structure-activity relationship for phosphorylations within the AT8 epitope, with a particular focus on residue S208 which was shown to trigger pathological states [9,10]. Although the global size of the mutant remains the same, we show that the phosphorylation of the AT8 epitope still modulates its local conformation. This methodology opens the way to study other pathological phosphorylations in other Tau regions, such as those recognized by the PHF-1 antibody. By systematically investigating the effects of phosphorylation on Tau's stability, and interactions with microtubules, a perspective of this work is to elucidate the molecular mechanisms underlying the loss of function associated with hyperphosphorylated Tau in neurodegenerative diseases.

Author contributions

CL, JM and P.B. designed the experiments. CSN and CB designed and prepared the unphosphorylated AT8 mutant and p-state 1 and 2 Tau mutants. CL and PB performed the DLS and UCA experiments and analyzed the data. JM performed all simulations, analyzed the data and modified the CALVADOS 2 IDRLab notebook to incorporate phosphorylation. DA and MT prepared WT Tau. CL performed the determination of the concentration of the mutants. CL and MM performed the EPR experiment and analyzed the data. EB, FXC and CSN performed and analyzed NMR

experiments. CL, JM, PB, CSN, CP and SSM participated in the scientific discussions. CL, JM and PB wrote the manuscript. MM and VB supervised the EPR experiments. All authors reviewed and corrected the manuscript.

Declaration of interest

The authors declare no competing interests.

Acknowledgement

This study was supported by the French Research Agency ANR-21-CE29-0024 MAGNETAU. This study was supported by the French Research Agency, the French government under the France 2030 investment plan, as part of the Initiative d'Excellence d'Aix-Marseille Université – AMIDEX "AMX-25-HAN-08", AMX-22-RE-V2-001 and by the LabEx DISTALZ (Development of Innovative Strategies for a Transdisciplinary approach to Alzheimer's disease, ANR-11-LABX-01). Additional support was provided by the "Initiative d'Excellence" program from the French State (Grant "DYNAMO", ANR-11-LABX-0011-01 and grant CACSICE, ANR-11-EQPX-0008). The authors are also grateful to the PINT platform facility available at the Institute of NeuroPhysiopathology, to Pavlo Shpak-Kraievskyi and Vecthorus for the accessibility to DLS device, Aix-Marseille Université, CNRS and the NMR and EPR facilities at the French Research Infrastructure INFRANALYTICS (FR2054) and the Aix-Marseille Université EPR center.

REFERENCES

1. Jack CR, Bennett DA, Blennow K, Carrillo MC, Dunn B, Haeberlein SB, et al. NIA-AA Research Framework: Toward a biological definition of Alzheimer's disease. Alzheimers Dement. 2018;14: 535–562. doi:10.1016/j.jalz.2018.02.018

2. Brion JP, Couck AM, Passareiro E, Flament-Durand J. Neurofibrillary tangles of Alzheimer's disease: an immunohistochemical study. J Submicrosc Cytol. 1985;17: 89–96.

3. Sillen A, Barbier P, Landrieu I, Lefebvre S, Wieruszeski J-M, Leroy A, et al. NMR Investigation of the Interaction between the Neuronal Protein Tau and the Microtubules. Biochemistry. 2007;46: 3055–3064. doi:10.1021/bi061920i

4. Goedert M, Spillantini MG, Jakes R, Rutherford D, Crowther RA. Multiple isoforms of human microtubule-associated protein tau: sequences and localization in neurofibrillary tangles of Alzheimer's disease. Neuron. 1989;3: 519–526. doi:10.1016/0896-6273(89)90210-9

5. Merino-Serrais P, Soria JM, Arrabal CA, Ortigado-López A, Esparza MÁG, Muñoz A, et al. Protein tau phosphorylation in the proline rich region and its implication in the progression of Alzheimer's disease. Exp Neurol. 2025;383: 115049. doi:10.1016/j.expneurol.2024.115049

6. Malia TJ, Teplyakov A, Ernst R, Wu S, Lacy ER, Liu X, et al. Epitope mapping and structural basis for the recognition of phosphorylated tau by the anti-tau antibody AT8. Proteins Struct Funct Bioinforma. 2016;84: 427–434. doi:10.1002/prot.24988

7. Braak H, Alafuzoff I, Arzberger T, Kretzschmar H, Del Tredici K. Staging of Alzheimer disease-associated neurofibrillary pathology using paraffin sections and immunocytochemistry. Acta Neuropathol (Berl). 2006;112: 389–404. doi:10.1007/s00401-006-0127-z

8. Gandhi NS, Landrieu I, Byrne C, Kukic P, Amniai L, Cantrelle F, et al. A Phosphorylation-Induced Turn Defines the Alzheimer's Disease AT8 Antibody Epitope on the Tau Protein. Angew Chem Int Ed. 2015;54: 6819–6823. doi:10.1002/anie.201501898

9. Despres C, Byrne C, Qi H, Cantrelle F-X, Huvent I, Chambraud B, et al. Identification of the Tau phosphorylation pattern that drives its aggregation. Proc Natl Acad Sci. 2017;114: 9080–9085. doi:10.1073/pnas.1708448114

10. Xia Y, Prokop S, Gorion K-MM, Kim JD, Sorrentino ZA, Bell BM, et al. Tau Ser208 phosphorylation promotes aggregation and reveals neuropathologic diversity in Alzheimer's disease and other tauopathies. Acta Neuropathol Commun. 2020;8: 88. doi:10.1186/s40478-020-00967-w

11. Kapcha LH, Rossky PJ. A Simple Atomic-Level Hydrophobicity Scale Reveals Protein Interfacial Structure. J Mol Biol. 2014;426: 484–498. doi:10.1016/j.jmb.2013.09.039

12. Tesei G, Schulze TK, Crehuet R, Lindorff-Larsen K. Accurate model of liquid–liquid phase behavior of intrinsically disordered proteins from optimization of single-chain properties. Proc Natl Acad Sci. 2021;118: e2111696118. doi:10.1073/pnas.2111696118

13. Rauh AS, Hedemark GS, Tesei G, Lindorff-Larsen K. A coarse-grained model for simulations of phosphorylated disordered proteins. Biophys J. 2026;125: 396–405. doi:10.1016/j.bpj.2025.07.001

14. Perdikari TM, Jovic N, Dignon GL, Kim YC, Fawzi NL, Mittal J. A predictive

coarse-grained model for position-specific effects of post-translational modifications. Biophys J. 2021;120: 1187–1197. doi:10.1016/j.bpj.2021.01.034

15. Marien J, Prévost C, Sacquin-Mora S. *n* P-Collabs: Investigating Counterion-Mediated Bridges in the Multiply Phosphorylated Tau-R2 Repeat. J Chem Inf Model. 2024;64: 6570–6582. doi:10.1021/acs.jcim.4c00742

16. Reboul E, Marien J, Prévost C, Taly A, Sacquin-Mora S. Menger_Curvature : a MDAKit implementation to decipher the dynamics, curvatures and flexibilities of polymeric backbones at the residue level. 2025. doi:10.1101/2025.04.04.647214

17. De Bessa T, Breuzard G, Allegro D, Devred F, Peyrot V, Barbier P. Tau Interaction with Tubulin and Microtubules: From Purified Proteins to Cells. In: Smet-Nocca C, editor. Tau Protein. New York, NY: Springer New York; 2017. pp. 61–85. doi:10.1007/978-1-4939-6598-4_4

18. Martinho M, Allegro D, Huvent I, Chabaud C, Etienne E, Kovacic H, et al. Two Tau binding sites on tubulin revealed by thiol-disulfide exchanges. Sci Rep. 2018;8: 13846. doi:10.1038/s41598-018-32096-9

19. El Hajjar L, Bridot C, Nguyen M, Cantrelle F-X, Landrieu I, Smet-Nocca C. Phosphorylation of Tau Protein by CDK2/cyclin A and GSK3β Recombinant Kinases: Analysis of Phosphorylation Patterns by Nuclear Magnetic Resonance Spectroscopy. In: Smet-Nocca C, editor. Tau Protein. New York, NY: Springer US; 2024. pp. 271–306. doi:10.1007/978-1-0716-3629-9_15

20. Schuck P. Size-Distribution Analysis of Macromolecules by Sedimentation Velocity Ultracentrifugation and Lamm Equation Modeling. Biophys J. 2000;78: 1606–1619. doi:10.1016/S0006-3495(00)76713-0

21. Philo JS. SEDNTERP: a calculation and database utility to aid interpretation of analytical ultracentrifugation and light scattering data. Eur Biophys J. 2023;52: 233–266. doi:10.1007/s00249-023-01629-0

22. Tesei G, Lindorff-Larsen K. Improved predictions of phase behaviour of intrinsically disordered proteins by tuning the interaction range. Open Res Eur. 2023;2: 94. doi:10.12688/openreseurope.14967.2

23. Tesei G, Trolle AI, Jonsson N, Betz J, Knudsen FE, Pesce F, et al. Conformational ensembles of the human intrinsically disordered proteome. Nature. 2024;626: 897–904. doi:10.1038/s41586-023-07004-5

24. Pesce F, Newcombe EA, Seiffert P, Tranchant EE, Olsen JG, Grace CR, et al. Assessment of models for calculating the hydrodynamic radius of intrinsically disordered proteins. Biophys J. 2023;122: 310–321. doi:10.1016/j.bpj.2022.12.013

25. Marien J, Prévost C, Sacquin-Mora S. Across (Conformational) Space and (Relaxation) Time: Using Coarse-Grain Simulations to Probe the Intra- and Interdomain Dynamics of the Tau Protein. J Phys Chem B. 2025;129: 12146–12158. doi:10.1021/acs.jpcb.5c06282

26. Rotkiewicz P, Skolnick J. Fast procedure for reconstruction of full-atom protein models from reduced representations. J Comput Chem. 2008;29: 1460–1465. doi:10.1002/jcc.20906

27. Humphrey W, Dalke A, Schulten K. VMD: Visual molecular dynamics. J Mol Graph. 1996;14: 33–38. doi:10.1016/0263-7855(96)00018-5

28. Huang J, Rauscher S, Nawrocki G, Ran T, Feig M, De Groot BL, et al. CHARMM36m: an improved force field for folded and intrinsically disordered proteins. Nat Methods. 2017;14: 71–73. doi:10.1038/nmeth.4067

29. Phillips JC, Hardy DJ, Maia JDC, Stone JE, Ribeiro JV, Bernardi RC, et al. Scalable molecular dynamics on CPU and GPU architectures with NAMD. J Chem Phys. 2020;153: 044130. doi:10.1063/5.0014475

30. Gowers R, Linke M, Barnoud J, Reddy T, Melo M, Seyler S, et al. MDAnalysis: A Python Package for the Rapid Analysis of Molecular Dynamics Simulations. Austin, Texas; 2016. pp. 98–105. doi:10.25080/Majora-629e541a-00e

31. Virtanen P, Gommers R, Oliphant TE, Haberland M, Reddy T, Cournapeau D, et al. SciPy 1.0: fundamental algorithms for scientific computing in Python. Nat Methods. 2020;17: 261–272. doi:10.1038/s41592-019-0686-2

32. Mukrasch MD, Bibow S, Korukottu J, Jeganathan S, Biernat J, Griesinger C, et al. Structural Polymorphism of 441-Residue Tau at Single Residue Resolution. Petsko GA, editor. PLoS Biol. 2009;7: e1000034. doi:10.1371/journal.pbio.1000034

33. Prince PR, Hochmair J, Brognaro H, Gevorgyan S, Franck M, Schubert R, et al. Initiation and modulation of Tau protein phase separation by the drug suramin. Sci Rep. 2023;13: 3963. doi:10.1038/s41598-023-29846-9

34. Le Breton N, Martinho M, Mileo E, Etienne E, Gerbaud G, Guigliarelli B, et al. Exploring intrinsically disordered proteins using site-directed spin labeling electron paramagnetic resonance spectroscopy. Front Mol Biosci. 2015;2. doi:10.3389/fmolb.2015.00021

35. Belle V, Rouger S, Costanzo S, Liquière E, Strancar J, Guigliarelli B, et al. Mapping α-helical induced folding within the intrinsically disordered C-terminal domain of the measles virus nucleoprotein by site-directed spin-labeling EPR spectroscopy. Proteins Struct Funct Bioinforma. 2008;73: 973–988. doi:10.1002/prot.22125

36. Cheek S, Zhang H, Grishin NV. Sequence and Structure Classification of Kinases. J Mol Biol. 2002;320: 855–881. doi:10.1016/S0022-2836(02)00538-7

37. Noble W, Hanger DP, Miller CCJ, Lovestone S. The Importance of Tau Phosphorylation for Neurodegenerative Diseases. Front Neurol. 2013;4. doi:10.3389/fneur.2013.00083

38. Kimura T, Sharma G, Ishiguro K, Hisanaga S. Phospho-Tau Bar Code: Analysis of Phosphoisotypes of Tau and Its Application to Tauopathy. Front Neurosci.

2018;12: 44. doi:10.3389/fnins.2018.00044

39. Gast K, Fiedler C. Dynamic and Static Light Scattering of Intrinsically Disordered Proteins. In: Uversky VN, Dunker AK, editors. Intrinsically Disordered Protein Analysis. New York, NY: Springer New York; 2012. pp. 137–161. doi:10.1007/978-1-4614-3704-8_9

40. Flach K, Hilbrich I, Schiffmann A, Gärtner U, Krüger M, Leonhardt M, et al. Tau Oligomers Impair Artificial Membrane Integrity and Cellular Viability. J Biol Chem. 2012;287: 43223–43233. doi:10.1074/jbc.M112.396176

41. Demeler B. Methods for the Design and Analysis of Analytical Ultracentrifugation Experiments. Curr Protoc. 2024;4: e974. doi:10.1002/cpz1.974

42. Devred F, Barbier P, Douillard S, Monasterio O, Andreu JM, Peyrot V. Tau Induces Ring and Microtubule Formation from αβ-Tubulin Dimers under Nonassembly Conditions. Biochemistry. 2004;43: 10520–10531. doi:10.1021/bi0493160

43. Amniai L, Barbier P, Sillen A, Wieruszeski J-M, Peyrot V, Lippens G, et al. Alzheimer disease specific phosphoepitopes of Tau interfere with assembly of tubulin but not binding to microtubules. FASEB J. 2009;23: 1146–1152. doi:10.1096/fj.08-121590

44. Lasorsa A, Merzougui H, Cantrelle F-X, Sicoli G, Dupré E, Hanoulle X, et al. Magnetic resonance investigation of conformational responses of tau protein to specific phosphorylation. Biophys Chem. 2024;305: 107155. doi:10.1016/j.bpc.2023.107155

45. Pierro A, Bonucci A, Magalon A, Belle V, Mileo E. Impact of Cellular Crowding on Protein Structural Dynamics Investigated by EPR Spectroscopy. Chem Rev. 2024;124: 9873–9898. doi:10.1021/acs.chemrev.3c00951

DATA ACCESSIBILITY

Raw coarse-grained pCALVADOS trajectories and minimized all-atom trajectories are available in the following Zenodo repository along with scripts allowing the conversion: https://doi.org/10.5281/zenodo.14900596.

pCALVADOS parameters and a jupyter notebook allowing to run a pCALVADOS simulation are available in the following Github repository:https://github.com/Jules-Marien/Articles/tree/main/_2025_Lohberger_Marien_pCALVADOS.

NMR chemical shift assignments of Tau AT8 mutant (from the 2N4R isoform) for 1H, 15N, and 13C backbone including N, HN, Cα, CO, and partial side chain (Cβ) resonances NMR resonances were deposited in the BioMagResBank (BMRB) with entry number 53407.